



141
143
THS

LIBRARY
Michigan State
University

This is to certify that the
dissertation entitled


STUDIES OF CURRENT INDUCED MAGNETIZATION REVERSAL
AND GENERATION OF GHz RADIATION IN MAGNETIC
NANOPILLARS.

presented by

Mustafa Yousef AlHajDarwish

has been accepted towards fulfillment
of the requirements for the

Ph.D. degree in Physics



-Major Professor's Signature

June 11, 2008

Date

PLACE IN RETURN BOX to remove this checkout from your record.
TO AVOID FINES return on or before date due.
MAY BE RECALLED with earlier due date if requested.

DATE DUE	DATE DUE	DATE DUE

**STUDIES OF CURRENT INDUCED MAGNETIZATION REVERSAL AND
GENERATION OF GHz RADIATION IN MAGNETIC NANOPILLARS.**

By

Mustafa Yousef AlHajDarwish

A DISSERTATION

**Submitted to
Michigan State University
in Partial fulfillment of the requirements
for the degree of**

DOCTOR OF PHILOSOPHY

Department of Physics and Astronomy

2008

ABSTRACT

STUDIES OF CURRENT INDUCED MAGNETIZATION REVERSAL AND GENERATION OF GHz RADIATION IN MAGNETIC NANOPILLARS.

By

Mustafa Yousef AlHajDarwish

This thesis describes studies of two phenomena: Current-Induced Magnetization Switching (CIMS), and Current-Induced Generation of GHz Radiation.

The CIMS part contains results of measurements of current-perpendicular-to-plane (CPP) magnetoresistance (MR) and CIMS behavior on Ferromagnetic/Non-metal/Ferromagnetic (F1/N/F2) nanopillars. Judicious combinations of F1 and F2 metals with different bulk scattering asymmetries, and with F1/N and N/F2 interfaces having different interfacial scattering asymmetries, are shown to be able to controllably, and independently, ‘invert’ both the CPP-MR and the CIMS. In ‘normal’ CPP-MR, $R(AP) > R(P)$, where $R(AP)$ and $R(P)$ are the nanopillar resistances for the anti-parallel (AP) and parallel (P) orientations of the F1 and F2 magnetic moments. In ‘inverse’ CPP-MR, $R(P) > R(AP)$. In ‘normal’ CIMS, positive current switches the nanopillar from the P to the AP state. In ‘inverse’ CIMS, positive current switches the nanopillar from AP to P. All four possible combinations of CPP-MR and CIMS—(a) ‘normal’-‘normal’, (b) ‘normal’-‘inverse’, ‘inverse’-‘normal’, and (d) ‘inverse’-‘inverse’ are shown and explained. These results rule out the self-Oersted field as the switching source, since the direction of that field is independent of the bulk or interfacial scattering asymmetries. Successful use of impurities to reverse the bulk scattering asymmetry shows the importance of scattering

off of impurities within the bulk F1 and F2 metals—i.e. that the transport must be treated as ‘diffusive’ rather than ‘ballistic’.

The GHz studies consist of five parts: (1) designing a sample geometry that allows reliable measurements; (2) making nanopillar samples with this geometry; (3) constructing a system for measuring frequencies up to 12 GHz and measuring current-driven GHz radiation data with it; (4) showing ‘scaling’ behavior of GHz data with the critical fields and currents for nominally identical (but actually slightly different) samples, and justifying such scaling; and (5) designing and constructing a system for frequency domain studies up to 40 GHz and for time domain studies.

DEDICATION

To the family of Mustafa AlHajDarwish.

ACKNOWLEDGMENTS

While completing the research program for his Ph.D. degree, Mustafa AlHajDarwish was stricken with cancer of the knee. This cancer led to replacement of his knee, then removal of his leg, and, finally, his untimely death. The continuing pain, plus debilitating effects of the operations, and extended chemotherapy before, between, and after the operations, precluded his writing his PhD thesis before his death.

His PhD guidance committee, considering his outstanding performance in formal classwork (grades all 4.0/4.0) and on subject examinations (three 4.0s and one 3.5), as well as his high quality research production, concluded that he merited a PhD degree. This research had led to 8 publications, two as first author, and included also design and construction of a new sample geometry and new measuring systems for studying dc current-induced microwave radiation, as well as obtaining new data with such samples.

Mustafa's advisor, Jack Bass, agreed to construct a PhD thesis by tying together what Mustafa had produced, with minimal connective material, and writing a brief abstract and a summary and conclusions. He was assisted by William P. Pratt Jr., who helped to supervise Mustafa's work, and by Amit Sharma, a PhD student in the process of writing his own thesis. Helpful comments were received from Norman O. Birge, S.D. (Bhanu) Mahanti, and members of Mustafa's guidance committee.

Mustafa was such an exceptional student, productive researcher, and wonderful person, that all who worked with him and assisted in the awarding of this PhD degree feel honored to have done so.

Thanks are given to the US National Science Foundation and to Seagate Technology Corporation for funding Mustafa and his research.

TABLE OF CONTENTS

List of Tables.....	vii
List of Figures.....	viii
1. Introduction.....	1
1.1. Background and Overview.....	1
1.2 Publications of Mustafa AlHaj Darwish.....	5
2. Inverted current-driven switching in Fe(Cr)/Cr/Fe(Cr) nanopillars.....	6
2.1 Background.....	6
2.2. Inverted current-driven switching in Fe(Cr)/Cr/Fe(Cr) nanopillars.....	10
3. Controlled normal and inverse current-induced magnetization switching and magnetoresistance in magnetic nanopillars.....	17
4. Spin-Transfer-Torque Generation of High Frequency (GHz) Radiation in Nanopillars: Sample Geometry, Measuring Systems, and Sample Data.....	31
4.1. Background.....	31
4.2. Sample Geometry.....	31
4.3. Measuring System to 12 GHz, Expected Behaviors, and Data.....	34
4.3.1. The Measuring System to 12 GHz.....	34
4.3.2. Expected Dynamical Motions.....	35
4.3.3. Experimental Data and an Example of Scaling.....	37
4.4. System for measuring GHz radiation up to 40 GHz and time domain studies.....	41
5. Summary and Conclusions.....	47
Bibliography.....	49

List of Tables

Table 3.1: F1/N/F2 for each figure, giving: the spin anisotropies (+ = positive, - = negative) of F1, F1/N, and their net anisotropy F1(Net), those of F2, N/F2, and their net anisotropy F2(Net), and the signs of the observed MR and CIMS (+ = normal and - = inverse).....	25
---	----

List of Figures.

- Fig. 2.1. As an addition for this thesis, we show data sets for Co/Au/Co at both 295K and 4.2K, measured by Mustafa AlHajDarwish, that could have been used as examples of ‘normal’ switching in place of Fig. 2.2 for Py/Cu/Py.....9
- Fig. 2.2. Py/Cu/Py data at 295K and 4.2K showing normal switching for dV/dI vs I at $H = 50$ Oe (main figures) and also for dV/dI vs H at $I = 0$ (insets). (From Urazhdin et al.²⁶).....15
- Fig. 2.3. Fe(Cr)/Cr/Fe(Cr) data at 295K and 4.2K showing inverted switching for dV/dI vs I at $H = 0$ (main figures) but normal dV/dI vs H at $I = 0$ (insets).....15
- Fig. 2.4. Fe(Cr)/Cr/Fe(Cr) data at 4.2K showing: (a) normal MR for dV/dI vs H at various I , but (b) inverted switching for dV/dI vs I at various H . Curves in (a) for $I \neq 0$ and in (b) for $H \neq 0$ are shifted vertically for clarity.....16
- Fig. 3.1. Py(24)/Cu(10)/Py(6) data at 295K (top) and 4.2K (bottom) showing normal MR (dV/dI vs H at $I = 0$) in the insets and normal CIMS for dV/dI vs I in the main figures at $H = 0$ Oe for 295K and at $H = 20$ Oe for 4.2K. In all figures, $I > 0$ is always from F1 to F2.....26
- Fig. 3.2. Fe(Cr)(30)/Cr(6)/Fe(Cr)(3.5) data at 295K (top) and 4.2K (bottom) showing normal MR (dV/dI vs H at $I = 0$) in the insets but inverse CIMS for dV/dI vs I at $H = 0$ in the main figures.....27
- Fig. 3.3. Py(20)/Cu(7)/Cr(3)/Fe(Cr)(3) data at 295K (top) and 4.2K (bottom) showing inverse MR (dV/dI vs H at $I = 0$) in the insets but normal CIMS for dV/dI vs I at $H = 0$ in the main figures.....28
- Fig. 3.4. Ni(Cr)(20)/Cu(20)/Py(10) data at 295K (top) and 4.2K (bottom) showing inverse MR (dV/dI vs H at $I = 0$) in the insets and inverse CIMS for dV/dI vs I at $H = 0$ in the main figures.....29
- Fig. 3.5. Py(24)/Cu(10)/Ni(Cr)(4) data at 4.2K showing inverse MR (dV/dI vs H at $I = 0$) in the inset and normal CIMS for dV/dI at $H = 0$ Oe in the main figure.....30
- Fig. 4.1 Sample configuration for GHz measurements. Each Si substrate contains 6 samples (lower left). Each sample has four Au contacts (lower right). Two of these Au contacts are grounds and two constitute 50 Ω strip lines (upper figure). Each sample can be contacted by a picoprobe coaxial cable pair in two ways as illustrated at the top and bottom of the upper figure.....33
- Fig. 4.2. Schematic drawings of a nanopillar (left), a sample with pico-probes (middle), and the system for measuring GHz radiation up to 12 GHz.....34

Fig. 4.3. The x,y,z. scale, and the direction of application of the magnetic field (top left). Three different monodomain motions of the free layer magnetization (assumed monodomain) (top middle and right). Frequencies expected for different applied magnetic fields (lower right).....	35
Fig. 4.4. Phase diagram as functions of applied magnetic field H (ordinate) and current I (abscissa) expected from monodomain analysis.....	36
Fig. 4.5. GHz radiation data from sample #2b5. Top: Examples of experimental 'phase diagrams' showing MR (upper left) and integrated power (upper right) as functions of H and I. Bottom: Examples of GHz peaks for fixed H = - 700 Oe and variable I (lower left) and for fixed I = 17 mA and variable H (lower right).....	38
Fig. 4.6. GHz radiation data from sample #2b3. Top: Examples of experimental 'phase diagrams' showing MR (upper left) and integrated power (upper right) as functions of H and I. Bottom: Examples of GHz peaks for fixed H = - 560 Oe and variable I (lower left) and for fixed I = 14 mA and variable H (lower right).....	39
Fig. 4.7. Power versus frequency plots comparing spectra for sample #1 and #2 at normalized values of H/H_C and $I/\Delta I_C$	40
Fig. 4.8. Schematic of the system for studying current-generated signals to 40 GHz.....	41
Fig. 4.9. Details of the system for both frequency studies to 40 GHz and time domain studies.....	43
Fig. 4.10. DC pulse generator.....	44
Fig. 4.11. Microwave pulse generator.....	45

Images in this dissertation are presented in color.

Chapter 1. Introduction

1.1. Background and Overview.

Mustafa AlHajDarwish came to Michigan State University (MSU) in 2000 after obtaining a Masters degree in Physics at Yarmouk University in Jordan. He came highly recommended, and his academic performance at MSU was outstanding: straight 4.0/4.0 in his coursework, and three 4.0s and one 3.5 on his comprehensive examinations. He began his Ph.D. research in 2001, initially contributing to two projects involving measurements of Current-Perpendicular-to-Plane (CPP) magnetoresistance (MR) of magnetic multilayers containing combinations of ferromagnetic (F) and Non-magnetic (N) metals. The first project involved a search for claimed mean-free-path effects in magnetic multilayers, and concluded that any such effects were not nearly as significant as had been claimed. The second project, a study of CPP-MR properties of Ru and Co/Ru interfaces, provided the first quantitative information about CPP-MR properties of a metal, Ru, that was beginning to be used to make artificial antiferromagnets for use in CPP-devices, and of the interfaces of Ru with the most widely used 'pure F-metal', Co. During these studies, Mustafa learned to prepare multilayers using a state-of-the art sputtering system, and to measure very small resistances at 4.2K using a unique superconducting-quantum device (SQUID) based bridge circuit.

After these preliminary studies, Mustafa started work on his Ph.D. thesis, which was planned to contain two parts, both involving magnetic multilayer nanopillars. Here, he learned to use a combination of optical and electron beam lithographies to make F/N/F nanopillars of typical dimensions $\sim 70 \text{ nm} \times 130 \text{ nm}$, and to measure both current-

induced magnetization switching (CIMS) and current induced generation of GHz radiation.

(1) In the first part, he succeeded in producing nanopillar multilayers with inverted current-induced magnetization switching (CIMS)—where positive current drives the magnetic order of the sample from anti-parallel (AP) to parallel (P), and negative current does the opposite. Mustafa's work here led to two publications, one in the Journal of Applied Physics and one in Physical Review Letters, which are included as chapters 2 and 3 of this PhD thesis. Further information about them, and the student who helped him with them, will be given at the start of chapter 2.

(2) The second part, the topic of Chapter 4, involved several tasks: (a) designing a new sample geometry for studying current-induced generation of GHz radiation, and making samples with this geometry; (b) assembling a system for measuring GHz radiation at frequencies up to 12 GHz using a borrowed spectrometer; (c) writing computer programs to control the massive data taking as functions of applied magnetic field H and applied DC current I ; (d) obtaining and analyzing good GHz data; and (e) designing and constructing a more flexible system for extending GHz measurements up to 40 GHz and for time domain studies. Having obtained experience in the topic by working for a summer at Seagate Technology, he succeeded in all parts. Unfortunately, however, by the time he obtained his first few data sets, he had been diagnosed with a bone cancer of the knee area, the effects of which progressively worsened, causing pain that quickly reduced his ability to carry out further research. Since there was no evidence that the cancer had spread beyond the leg, after a period of chemotherapy, he decided with his doctors to have the knee and part of the thigh-bone removed in hopes of

eliminating the cancer. The operation appeared to be successful, and was followed by months of additional chemotherapy during which he was mostly incapacitated. Again, unfortunately, by the end of the treatment it became clear that the cancer had not been completely eliminated and he and his doctors decided that the best hope was to remove the leg up to the thigh. He underwent another operation and further chemotherapy. For a while it looked as if this treatment might be successful. But in the end the cancer spread further, and finally took his life.

The thesis that is presented includes both parts, however with the second part not as extensive as it would have been absent his illness. The guidance committee judges that this totality, combined with his outstanding academic performance, are more than sufficient to justify the awarding of a Ph.D. degree.

Given the unusual circumstances of this thesis, it was decided to describe the work that he did, specifying clearly and completely his contributions, but adding only the minimum of connective material to tie together his work.

The thesis consists of the following four chapters.

Chapter 1. **Background and Overview.** This chapter contains some background and an overview of the thesis, plus a list of Mustafa's publications

Chapter 2. **Inverted current-driven switching in Fe(Cr)/Cr/Fe(Cr) nanopillars.** This chapter contains a brief rationale for the study of Inverted Current-driven Switching, and then the text of the first publication, a study of Fe/Cr/Fe multilayers.

Chapter 3. **Controlled normal and inverse current-induced magnetization switching and magnetoresistance in magnetic nanopillars.** This chapter contains the second publication on inverting CIMS, which extended data to several additional F/N/F

structures, and was designed to test the importance of contributions from the bulk F-metals and the F/N interfaces. .

Chapter 4. Spin-Transfer-Torque Generation of High Frequency (GHz) Radiation in Nanopillars: Sample Geometry, Measuring Systems, Data Taking, and Sample Data. This chapter contains descriptions of: (4.1) The sample geometry that Mustafa helped to develop; (4.2) The measuring system for taking data up to 12 GHz, examples (prepared by Mustafa) of the expected phenomena, and some data (taken by Mustafa), including an illustration of his discovery that the data could be ‘scaled’ to make manifest similarities of data from nominally identical, but actually slightly different, samples; (4.3) the system that Mustafa helped to design and construct for extending measurements to 40 GHz and for time domain studies. Mustafa also wrote programs for data taking and analysis. Since those programs are complex, and inappropriate for inclusion, we simply note here that he wrote them, and omit them from the thesis.

1.2. Publications of Mustafa AlHaj Darwish (MAHD).

Bold = experiments that MAHD led. **Unbold** = experiments to which he contributed.

1. Absence of Mean-Free-Path Effects in CPP Magnetoresistance of Magnetic Multilayers. (K. Eid, D. Portner, J. Borchers, R. Loloee, M. AlHaj Darwish, M. Tsoi, H. Kurt, K.V. O'Donovan, W.P Pratt Jr., and J. Bass), Phys. Rev. **B65**, 054424 (2002).
2. Current-perpendicular-to-plane Magnetoresistance Properties of Ru and Co/Ru Interfaces, (K. Eid, R. Fonck, M. AlHajDarwish, W.P. Pratt Jr., and J. Bass), J. Appl. Phys. **91**, 8102 (2002).
3. **Inverted Current-Driven Switching in Fe(Cr)/Cr/Fe(Cr) Nanopillars**, (M. AlHajDarwish, A. Fert, W.P. Pratt Jr., and J. Bass), J. Appl. Phys. **95**, 6771 (2004).
4. Current-induced magnetization Dynamics in Current Perpendicular to the Plane Spin Valves, (M. Covington, M. AlHajDarwish, Y. Ding, et al.), Phys. Rev. **B69**, 184406 (2004).
5. **Controlled Normal and Inverse Current-Induced Magnetization Switching and Magnetoresistance in Magnetic Nanopillars**, (M. AlHajDarwish, H.Kurt, S. Urazhdin, A. Fert, R. Loloee, W.P. Pratt Jr., and J. Bass), Phys. Rev. Lett. **93**, 157203 (2004).
6. Spin Transfer Effects in Current perpendicular to the Plane Spin Valves, (M. Covington, M. AlHajDarwish, Y. Ding, et al.), J. Magn. Magn. Mat. **287**, 325 (2005).
7. Manipulating Current-Induced Magnetization Switching, (S. Urazhdin, H. Kurt, M. AlHajDarwish, N.O. Birge, W.P. Pratt Jr., and J. Bass), J. Appl. Phys. **97**, 10C701 (2005).
8. Effect of asymmetric leads on critical switching current in magnetic nanopillars. (H. Kurt, M. AlHajDarwish, W.P. Pratt Jr., and J. Bass), Appl. Phys. Lett. **89**, 082513 (2006).

Chapter 2. Inverted current-driven switching in Fe(Cr)/Cr/Fe(Cr) nanopillars.

2.1. Background

The work in both Chapters 2 and 3 involved use of a lock-in amplifier for ac measurements of dV/dI on F/N/F nanopillars as functions of applied magnetic field H for applied DC current $I = 0$ (CPP-MR), and of applied DC I for applied magnetic field $H = 0$ (CIMS). Fig. 2.1 contains examples of ‘normal’ CPP-MR and ‘normal’ CIMS data for a Co(30nm)/Au(10nm)/Co(4nm) nanopillar that Mustafa both prepared and measured. The ‘top’ part of the nanopillar, consisting of the thinner (here 4 nm thick Co) layer and a nominal half of the separating layer (here Au), was patterned to nanopillar size (typically $\sim 70 \text{ nm} \times 130 \text{ nm}$) and the ‘bottom’ part, composed of the rest of the separating layer and the thicker (here 30 nm thick Co) were left unpatterned. Application of a large in-plane magnetic field H , with DC current $I \approx 0$, will put the sample into a parallel (P) orientation of the magnetizations M of the two F-layers, both pointing along the field. When the field H is reversed, the thicker layer will reverse at smaller H than the thinner layer, giving a temporary antiparallel (AP) orientation of the two magnetizations, before the thinner layer reverses in larger H . In contrast, for $H \approx 0$, application of a large DC I will affect only the thinner F-layer, due to its smaller volume and the much larger current density that it experiences. The top part of Fig. 2.1 (CPP-MR) shows dV/dI vs H for $I_{dc} = 0$. Normal CPP-MR means that $dV/dI(\text{AP})$ is larger in the state where the magnetic moments of the two F-layers are aligned anti-parallel (AP) to each other than $dV/dI(\text{P})$ in the state where the moments are aligned parallel (P) to each other. Note that dV/dI vs H

is symmetric about $H = 0$. The bottom part of Fig. 2.1 (CIMS) shows dV/dI vs I_{dc} for $H = 0$. Normal CIMS means that positive I (defined as electrons flowing from the thinner ‘switching’ F-layer to the thicker ‘fixed’ F-layer) drives the sample magnetic order to AP, and negative I (electrons flowing from the thicker F-layer to the thinner one) drives the system to the P-state. Thus dV/dI vs I_{dc} is asymmetric about $I = 0$. Note that the values of $dV/dI(AP)$ and $dV/dI(P)$ are closely the same for the CPP-MR and CIMS, showing that the nanopillar switches in both cases between fully AP and fully P states.

By the time these experiments were undertaken, most researchers accepted that the asymmetry of the CIMS switching in Fig. 2.1, meant that the CIMS switching could not be due primarily to the self-Oersted field of the large DC current I , because should a field should produce effective ‘P-like’ states at both large $+H$ and large $-H$ (we say ‘effective’ P-like, because the circular field of a linear I should produce stable vortex-like final states). However, some were still not convinced, and one of the purposes of these experiments was to address this issue in a new way.

The purposes of the studies in the two papers below were, thus, two-fold. One was to test unequivocally for dominance of CIMS, in that the self-Oersted field cannot produce inverted CIMS, since its direction is independent of the specific scattering asymmetries of the F metal and F/N interfaces. The other was to see if samples containing F and N metal pairs with different bulk and interfacial scattering anisotropies would behave as predicted by the original simple Slonczewski ‘ballistic’ model of CIMS, or if one could distinguish effects of ‘spin-accumulation’ in the nanopillars. Said another way, to see if transport in the samples was better treated as ‘ballistic’ (original Slonczewski) or ‘diffusive’ (later models). Showing that CIMS could be qualitatively changed by

alloying the F-metal would be strong evidence in favor of diffusive transport. Details of the samples and their behaviors, and the conclusions reached, are given in the two papers.

All of the samples involving Fe and Cr in both Chapters 2 and 3 were made and measured by Mustafa. As shown in Fig. 1.1, Mustafa also measured simple ‘normal’ CIMS samples comparable to the Py/Cu/Py samples included in Chapters 2 and 3. The Py/Cu/Py data were chosen because we had already published a complete study of such samples in ref. [26] below, and we used Mustafa’s new samples of Py/Cu/Cr/Fe(Cr) samples in Chapter 3. The remaining samples in Chapter 3 were made by Huseyin Kurt and studied jointly by Mustafa and Kurt. These samples were included in the earlier Ph.D. thesis of Huseyin Kurt.

Normal switching in Co30nm/Au10nm/Co4nm Nanopillars

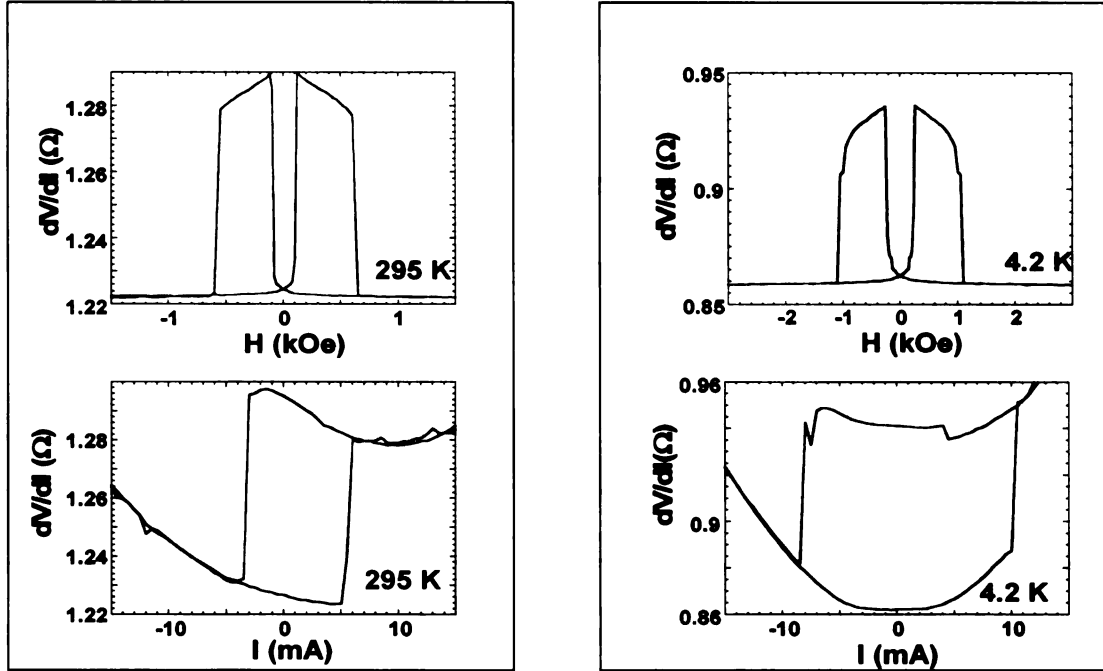


Fig. 2.1. As an addition for this thesis, we show CPP-MR (top) and CIMS (bottom) data for Co/Au/Co at both 295K (left) and 4.2K (right), measured by Mustafa AlHajDarwish, that could have been used as examples of ‘normal’ switching in place of Fig. 2.2 for Py/Cu/Py in the following paper.

2.2. Inverted current-driven switching in Fe(Cr)/Cr/Fe(Cr) nanopillars.

M. AlHajDarwish,¹ A. Fert,² W.P. Pratt Jr.,¹ and J. Bass¹

[1] Department of Physics and Astronomy, Center for Sensor Materials, Center for Fundamental Materials Research, Michigan State University, East Lansing, MI, USA 48824-2320.

[2] Unite Mixte de Physique, CNRS/THALES, Orsay, France 91404.

From both theory and experiment, scattering of minority electrons is expected to be weaker than scattering of majority electrons in both dilute Fe(Cr) alloys and at Fe(Cr)/Cr interfaces. We show that Fe(Cr)/Cr/Fe(Cr) trilayer nanopillars display a normal magnetoresistance—i.e., largest resistance at low magnetic fields and smallest at high fields, but an inverted current-driven switching—i.e., positive current flowing from the fixed to the reversing layer switches the trilayer from higher to lower resistance, and negative current switches it from lower to higher.

Reprinted with permission from M. AlHajDarwish, A. Fert, W.P. Pratt Jr., and J. Bass, J. Appl. Phys. **95**, 6771 (2004), Copyright 2004, American Institute of Physics.

There is great interest in current-driven magnetic switching in nanofabricated ferromagnetic/non-magnetic/ferromagnetic (F/N/F) trilayers, both to understand the underlying physics and for device potential.¹⁻²⁷ For simplest switching, one F-layer (pinned) is made much thicker (and sometimes with larger area) than the other. An applied dc current then reverses only the thinner (and sometimes smaller) F-layer (free). In all nanopillars studied so far, minority electrons were scattered more strongly than majority ones both within the F-layers and at the F/N interfaces. In such a case, a positive current flowing in the spacer layer from the thick pinned layer to the thin free one is positively polarized in the frame of the thick layer (i.e. its magnetic moment is parallel to the magnetization of the pinned layer). Large enough positive current was then found to cause the free layer's magnetic moment to rotate anti-parallel (AP) to that of the pinned layer, and reversed (negative) current caused it to rotate parallel (P). Because the scattering was the same (strongest for minority electrons) within both F-metals and at all F/N interfaces, the resistance of the trilayer was largest in the AP state at low magnetic fields H and smallest in the P state at high H , corresponding to a normal magnetoresistance (MR).²⁸ Sufficiently large positive current then produced a step increase in resistance and sufficiently large negative current a step decrease, which, together, we call normal switching.

If, however, majority electrons are scattered more strongly both within the pinned F-metal layer and at its F/N interface, the direction of polarization of the exiting current should reverse—i.e. positive current should be negatively spin-polarized. Published models imply that negatively-polarized positive current impinging upon the free layer should cause its moment to rotate P to that of the pinned layer,^{1,2} and negative current

should cause the moment of the free layer to rotate AP. If the two F layers are identical, the field-driven magnetoresistance (MR) should remain normal, with larger resistance in the low field AP-state than in the high field P-state.²⁸ However, the current-driven switching should ‘invert’, in that positive current should drive the system from the higher resistance AP state to the lower resistance P state, and negative current the opposite.

Together, theory and experiment²⁹⁻³³ indicate that both a dilute Fe(Cr) alloy and an Fe(Cr)/Cr interface should scatter majority electrons more strongly. In this paper we show that an Fe(Cr)/Cr/Fe(Cr) trilayer displays the two behaviors described in the previous paragraph, namely a normal MR—resistance smallest in the high field P-state, but an inverted current-driven switching—positive current drives the system to the lower resistance P state and negative to the higher resistance AP state

Magnetic nanopillars of approximately elliptical shape and dimensions ~ 70 nm x 130 nm were prepared by triode sputtering onto Si substrates.^{26,27} The Fe(Cr) alloy contained ~ 5 at.% Cr. The multilayers consisted of a thick Cu lower contact, a 30 nm pinned Fe(Cr) layer, a 6 nm thick Cr layer, a 3.5 nm thick ‘free’ Fe(Cr) layer, and a thick Au top contact. To minimize dipolar coupling between the Fe(Cr) layers, the sample was ion-milled through part of the Cr layer, so as to leave the bottom (pinned) Fe(Cr) layer wide. With this geometry, the wide layer ‘switches’ upon application of a relatively small magnetic field, but does not switch upon application of a current large enough to switch the patterned top (free) Fe(Cr) layer. Differential resistances, dV/dI , were measured with four probes and lock-in detection, adding an ac current of ~ 20 μ A at 8 kHz to the dc current I . H is directed along the easy axis of the nanopillar.

As a comparison standard for our Fe(Cr)/Cr/Fe(Cr) data, Fig. 2.2 shows previously published data [26] for dV/dI vs I at $H = 50$ Oe and dV/dI vs H at $I = 0$ for nanopillars of Py/Cu/Py (Py = Permalloy = $\text{Ni}_{84}\text{Fe}_{16}$), where positive current was defined the same as in the present paper. The dV/dI vs I data are shown full size, and the dV/dI vs H (i.e., MR) data as insets in the top center. The upper curves are for room temperature (295K) and the lower ones for 4.2K. Both the MR and dV/dI vs I curves for Py/Cu/Py are ‘normal’—i.e. dV/dI is smallest in the high field P state, and positive current switches the sample from its low resistance (P) state to its high resistance (AP) state, and vice versa for negative current. In the MR curves at both temperatures, the transitions from the P to AP states occur only after the magnetic field passes through zero, consistent with weak magnetic coupling.

Fig. 2.3 shows our new data for Fe(Cr)/Cr/Fe(Cr) trilayers. The changes in dV/dI vs I or H for Fe(Cr)/Cr/Fe(Cr) are considerably smaller than those for Py/Cu/Py, but still visible. As expected, the MR curves at $I = 0$ are still ‘normal’—i.e., smallest in the P state. And, similarly to Py/Cu/Py, the MR transitions from the P to AP states appear only after the magnetic field passes through zero. In contrast to the similar MR curves in Figs. 2.2 and 2.3, the dV/dI vs I curves for the Fe(Cr)/Cr/Fe(Cr) samples behave oppositely to those for Py/Cu/Py. Positive I switches the Fe(Cr) free layer from the high resistance AP to the low resistance P state, and negative I switches it from the P to AP state. The dV/dI vs I curves for Fe(Cr)/Cr/Fe(Cr) are ‘inverted’ from the ‘normal’ behavior for Py/Cu/Py. In all cases in both Fig. 2.2 and Fig. 2.3, the agreement between the minimum and maximum values of dV/dI , together with almost single step switching (e.g., at -11 and $+$

6 ma at 4.2K), show that the current-driven switching is complete. Normal MRs and inverted current-driven switching were also seen in other Fe(Cr)/Cr/Fe(Cr) samples.

We also checked that similar results were obtained for the MR with $I \neq 0$ and for dV/dI vs I for $H \neq 0$. Fig. 2.4 shows how dV/dI vs H and dV/dI vs I change at 4.2K for the same Fe(Cr)/Cr/Fe(Cr) trilayer when we vary H at fixed I (Fig. 2.4a) and I at fixed H (Fig. 2.4b). In part because the jumps in dV/dI are small, the switching is irregular and often partial. But all dV/dI vs H switching seen is normal, and all dV/dI vs I switching seen (both hysteretic and reversible) is inverted. Asymmetry in H is presumably due to a combination of the self-Oersted field and sample shape asymmetry.

To summarize, we have shown that Fe(Cr)/Cr/Fe(Cr) trilayers give normal MR—smallest dV/dI vs H at high fields when the magnetizations of the two Fe(Cr) layers are aligned parallel (P) to each other, but inverted dV/dI vs I —large positive current causes switching from the AP to the parallel (P) state and large negative current causes switching from the P to the AP state.

Acknowledgments: The authors thank S. Urazhdin for helpful suggestions and for permission to use his published Py/Cu/Py data in this paper. This research was supported in part by the MSU CFMR, CSM, the MSU Keck Microfabrication Facility, NSF grants DMR 02-02476, 98-09688, NSF-EU collaborative grant 00-98803, and Seagate Technology.

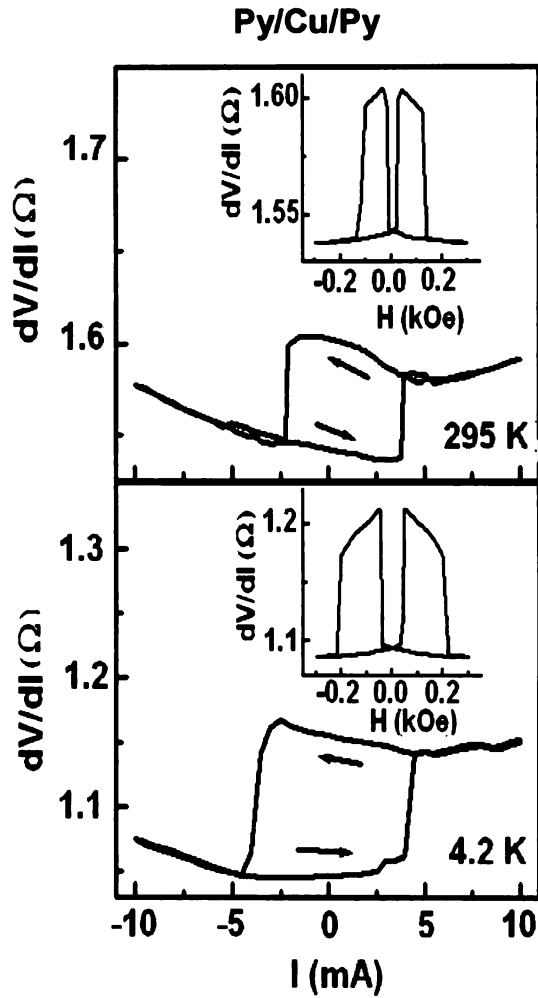


Fig. 2.2. Py/Cu/Py data at 295K and 4.2K showing normal switching for dV/dI vs I at $H = 50$ Oe (main figures) and also for dV/dI vs H at $I = 0$ (insets). (From Urazhdin et al. [26]).

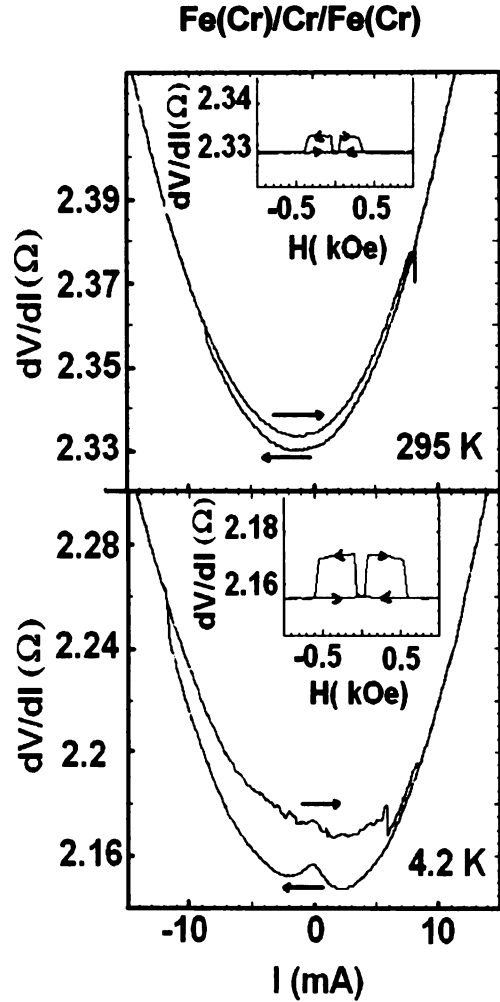


Fig. 2.3. Fe(Cr)/Cr/Fe(Cr) data at 295K and 4.2K showing inverted switching for dV/dI vs I at $H = 0$ (main figures) but normal dV/dI vs H at $I = 0$ (insets).

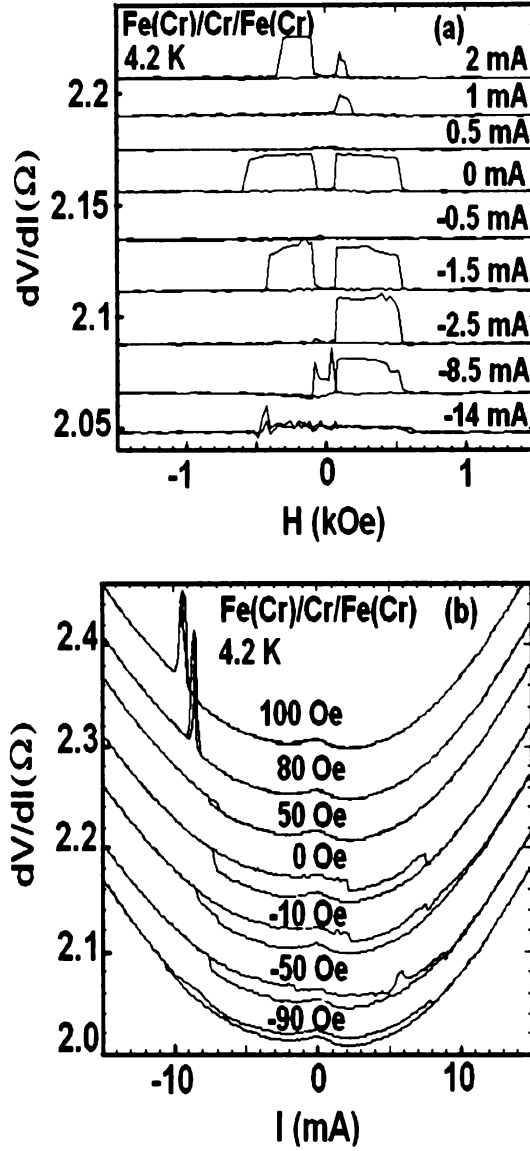


Fig. 2.4. Fe(Cr)/Cr/Fe(Cr) data at 4.2K showing: (a) normal MR for dV/dI vs H at various I , but (b) inverted switching for dV/dI vs I at various H . Curves in (a) for $I \neq 0$ and in (b) for $H \neq 0$ are shifted vertically for clarity.

Chapter 3. Controlled normal and inverse current-induced magnetization switching and magnetoresistance in magnetic nanopillars.

M. AlHajDarwish,¹ H. Kurt,¹ S. Urazhdin,¹ A. Fert,² R. Loloee, W.P. Pratt Jr.,¹ and J.

Bass¹

[1] Department of Physics and Astronomy, Center for Sensor Materials, Center for Fundamental Materials Research, Michigan State University, East Lansing, MI, USA

48824-2320.

[2] Université Paris-Sud and Unite Mixte de Physique, CNRS/THALES, Orsay, France

91404.

By combining pairs of ferromagnetic metals with the same or different signs of scattering anisotropies in ferromagnetic/non-magnetic/ferromagnetic metal nanopillars, we independently invert just the magnetoresistance, just the direction of current-induced magnetization switching, or both together, at room temperature (295K) and at 4.2K. In all cases studied, the switching direction is correctly predicted from the net scattering anisotropy of the fixed ferromagnet, including both bulk and interfacial contributions.

Reprinted with permission from M. AlHajDarwish, H.Kurt, S. Urazhdin, A. Fert, R. Loloee, W.P. Pratt Jr., and J. Bass, Phys. Rev. Lett. **93**, 157203 (2004), Copyright 2004, American Physical Society.

The magnetization of a ferromagnetic (F) metal can be reversed by spin transfer from a spin-polarized current, i.e., without applying a magnetic field [1-4]. Such Current-Induced Magnetization Switching (CIMS) [1-7,9,12,13,15,23,26,27,34-45] has been seen in (F1/N/F2) trilayer nanopillars in which the spin polarized current prepared with a thicker layer F1 passes through a non-magnetic metal (N) and switches the moment of a thinner layer F2. CIMS is promising for switching small magnetic devices (e.g., magnetic random-access-memory, MRAM), and also raises subtle fundamental issues.

Although CIMS is expected to result from spin polarization of the current, it has yet to be shown that CIMS can be manipulated (e.g., inverted) by changing that polarization. In prior studies, minority electrons were scattered more strongly in F1, F2 and at F1/N and N/F2 interfaces (positive spin anisotropy). The current is then always positively spin-polarized in the F-layers, i.e., carried mainly by majority spin electrons. In these “standard” conditions, electrons flowing from F1 to F2 (negative charge current, $I < 0$) switch the moment **M2** of F2 from antiparallel (AP) to **M1** (high resistance R) to parallel (P) to **M1** (low R). Conversely, positive $I (> 0)$ switches F2 from P to AP. We call these behaviors ‘normal’ CIMS and ‘normal’ current-perpendicular-to-plane (CPP) magnetoresistance (MR).

We present CIMS experiments exploiting the possibility of inverting the spin anisotropy by doping F1, F2, or both together, with an impurity (Cr) that scatters majority spin electrons more strongly [28,29,31,32,33,46-48]. We thus show, for the first time, that inversion of the spin anisotropy can invert the CIMS direction, i.e., invert the signs of I for AP to P and P to AP transitions. We also find inversions of the MR (larger R for P state) with appropriately doped samples, as expected from prior CPP-MR results

at low temperature [28,29]. Measurements at 295K and 4.2K show that the qualitative behaviors of both CIMS and MR are independent of temperature over this range.

Analysis of the switching behaviors lets us discriminate between different models of CIMS. We divide the standard models of the spin-transfer-torque (STT) used to describe CIMS into two classes, ballistic [1,3,37] and diffusive [2,4,12,13,41,45,49]. Both predict that changing scattering anisotropies can invert the MR and/or CIMS. However, expectations for the two need not agree. In ballistic transport, the spin anisotropy comes only from reflections at the F/N interfaces. Inverting CIMS is predicted to require negative anisotropy at F1/N [37]. Inverting the MR should require opposite scattering anisotropies at F1/N and N/F2 [28]. In diffusive transport, the spin anisotropy of scattering within the F-layers is also important, so that one must consider the net anisotropy of a given F-layer (e.g., the resultant effect of the bulk of F and its F/N interface). An additional effect, spin accumulation, can also either support or compete with the effect of polarized current [2,4,12,13,41,45,49]. In addition to determining the relation between spin anisotropies and CIMS direction, we will answer the following questions relevant to understanding CIMS. (a) Is the CIMS direction set only by interface scattering anisotropy? No. (b) Can impurity scattering within the layers be important? Yes. (c) Do the anisotropies of F1 and F2 play different roles for the CIMS direction of F2? Yes. (d) Can spin-accumulation be important? Yes.

To determine how changing spin anisotropies changes CIMS directions, we combine in different ways three pairs of materials: Py/Cu (Py = $\text{Ni}_{84}\text{Fe}_{16}$) where both bulk and interface anisotropies are positive [28]; Fe(Cr)/Cr (Fe(Cr) = $\text{Fe}_{95}\text{Cr}_5$), where both are negative [29,31,32,33,46-48]; and Ni(Cr)/Cu (Ni(Cr) = $\text{Ni}_{97}\text{Cr}_3$), where the Ni(Cr) is

thick enough so its negative anisotropy dominates the positive anisotropy of the interface [50]. The net anisotropy is determined using the MR. Comparing Fe(Cr)/Cr with Ni(Cr)/Cu for F1 or F2 explicitly tests the importance of interface anisotropies. Table 3.1 lists the signs for F1, F2 bulk, F1/N, N/F2 interfaces, and F1(net), F2(net), as well as for the observed MR and CIMS.

Our sample preparation and measurement techniques are described elsewhere [26,27]. Our multilayers were triode sputtered onto Si substrates, and patterned into nanopillars of approximately elliptical shape and dimensions $\sim 70 \text{ nm} \times 130 \text{ nm}$. The samples consisted of a thick Cu lower contact, the multilayer, and a thick Au top contact. The N-layer was made thick (6-20 nm) to minimize exchange coupling between F1 and F2. To simplify switching, samples were ion-milled only through F2 and part of N, leaving F1 (fixed polarizer) to have much larger area ($\sim \mu\text{m}^2$) and to be thicker than F2. Dipolar coupling between F1 and F2 is then minimal, and H (along the nanopillar easy axis) reverses **M1** and **M2** sequentially, but I reverses only **M2** of F2 (free switcher). For each combination of MR and CIMS, the switching direction is the same at 295K and 4.2K. Each switching behavior was also independently reproduced, and no inconsistent switching was seen.

Py and Py/Cu interfaces both have positive scattering anisotropy [28]. In agreement with prior data [26,27], Fig. 3.1 shows that Py(24)/Cu(10)/Py(6) nanopillars (layer thicknesses are in nm) give normal MR and normal CIMS. At both 295K and 4.2K, the MR transitions from P to AP occur after H passes through zero, consistent with little or no magnetic coupling. The agreement between the minimum and maximum values of dV/dI for the MR and current-driven curves also shows that the switching is complete. Figs. 3.2-3.5 show similarly weak coupling and complete switching.

In contrast to Py and Py/Cu, Fe(Cr) and Fe/Cr interfaces both have negative scattering anisotropies [29,31,32,33,46-48]. Since F1 and F2 are the same alloy, Fe(Cr)(30)/Cr(6)/Fe(Cr)(3.5) nanopillars should give normal MR [28,29]. Fig. 3.2 shows that they do, and also give inverse CIMS. The changes in dV/dI vs I or H are smaller than for Py/Cu/Py, due to spin-memory-loss in the Cr(6) layer [47] and smaller scattering anisotropy of Fe(Cr) [29]. More Fe(Cr)/Cr/Fe(Cr) data are given in [46].

Fig. 3.3 shows data for the four component system Py(20)/Cu(7)/Cr(3)/Fe(Cr)(3). Combining the net positive scattering anisotropy for F1 with the net negative anisotropy for F2 gives the expected inverse MR [28,29]. But the CIMS is normal— $I > 0$ switches from P to AP—remembering that inverse MR means largest resistance in the P state.

Fig. 3.4 shows the fourth case, Ni(Cr)(20)/Cu(20)/Py(10). Combining net negative anisotropy for Ni(Cr) with net positive anisotropy for Py gives the expected inverse MR, and now inverse CIMS.

Fig. 3.5 shows another way to achieve inverse MR with normal CIMS, using Py(24)/Cu(10)/NiCr(4). In Figs. 3.3 and 3.5, this same combination of MR and CIMS occurs with opposite F2 interface anisotropies—negative in Fig. 3.3 but positive in Fig. 3.5.

Lastly, in Figs 3.2 and 3.4, opposite interface anisotropies for F1 don't change the CIMS direction.

Before comparing our data with theory, we summarize the results in Figs. 3.1-3.5. As expected for the MR [28,29], when the net scattering anisotropies for F1 and F2 are the same (Figs. 3.1, 3.2), the MR is normal, and when they are opposite (Figs. 3.3-3.5), the

MR is inverse. New for CIMS, when the net scattering anisotropy for F1 is positive, CIMS is normal (Figs. 3.1,3.3,3.5), and when it is negative (Figs. 3.2,3.4), CIMS is inverse. For these samples, the direction of CIMS is set by the net scattering anisotropy of F1 and is independent of that of F2. Comparing Figs. 3.3 and 3.5, and Figs. 3.2 and 3.4, shows that, when bulk scattering predominates, the CIMS direction is independent of the scattering anisotropy of F1/N and N/F2. Finally, dominance of the bulk contribution of scattering anisotropy in either F1 (e.g., Ni(Cr) in Fig. 3.4) or F2 (Ni(Cr) in Fig. 3.5) is inconsistent with ballistic transport through the nanopillar, where the interfaces must dominate the scattering.

As just noted, ballistic STT models cannot describe our data involving Ni(Cr). Intriguingly, however, the CIMS directions in Figs. 3.1-3.5 accord with the ballistic prediction of [37], if the scattering anisotropy at the F1/N interface is simply replaced by the net anisotropy for F1. This last result also follows directly from the non-STT model of ref. [44].

For diffusive transport, the current polarization in N depends upon the net scattering anisotropies of both F1 and F2, and CIMS depends upon both the spin polarized charge current and spin-accumulation effects [2,4,12,41,45]. Eq. 3.1 reproduces Eq. 5 of ref. [45] for the torque Γ^P at a small angle from the P state (for Γ^{AP} , replace P by AP). Note that our notations for F1 and F2 are reversed from [45].

$$\Gamma^P / \hbar = [\{(v_F m_N^P)/8 + (j_{m,N}^P)/2\}(1 - e^{-t_N/\lambda_N}) + \{(v_F m_{F1}^P)/4 + j_{m,F1}^P\} e^{-t_N/\lambda_N}] (\mathbf{M}_2 \mathbf{x} (\mathbf{M}_2 \mathbf{x} \mathbf{M}_1)) \quad (3.1)$$

Eq. 3.1 comes from an extension of the Valet-Fert [51] model of CPP-MR to non-colinear states. v_F is the Fermi velocity in N, m_N^P and $j_{m,N}^P$ are the spin accumulation density [15,16,19,30] and spin current density in N just outside the F2/N interface calculated for the P state, m_{F1}^P and $j_{m,F1}^P$ are the same quantities in F1 just inside the F1/N interface, and t_N and λ_N are the thickness and mean-free-path of N. The second { } parenthesis dominates in the usual case where $t_N \ll \lambda_N$ and the first dominates if $t_N \gg \lambda_N$. In both cases, the signs of spin-current and spin-accumulation can support each other or compete.

Using the best available parameters from CPP-MR experiments [28,47,50], we calculate spin currents and spin accumulations [28,51], and then insert these into Γ^P or Γ^{AP} . In all cases except Fig. 3.4, the signs of spin current and accumulation agree and are the same as those expected from the sign of the net spin anisotropy of F1 seen by MR. The situation for Fig. 3.4 is more complex. For P to AP, the spin accumulation dominates Γ^P and gives the observed inverse CIMS at $I < 0$; because of the particular parameters of Ni(Cr) and Py, for this case the spin current alone would predict normal CIMS. For AP to P, the spin current dominates Γ^{AP} and gives the observed inverse CIMS at $I > 0$. Thus, we reproduce the behaviors in Fig. 3.4.

To summarize, we have shown that judiciously chosen pairs of ferromagnetic (F) metals or ferromagnetic alloys can produce all four combinations of normal and inverse MR and current-induced magnetization switching (CIMS) at both 4.2K and 295K. The MR is normal if the net scattering anisotropies of F1 and F2 have the same sign, and inverse if they don't. For the samples studied, the CIMS direction is determined solely

by the net anisotropy for F1, although in Fig. 3.4 this result requires dominance of spin-accumulation for the P to AP transition. This latter result, as well as the inverted MRs in Figs. 3.4 and 3.5, show that the interpretation of MR and CIMS must generally take account not only of the interface scattering assumed in ballistic models, but also scattering (and diffusion) within the F-layers. As the widely accepted mechanism of CIMS is a quasi-interfacial absorption of the transverse component of the spin current [1,12,37,41,45], the importance of scattering within the F-layers might seem surprising. However, in a non-collinear magnetic configuration, the transverse spin current in the frame of F2 is related to the longitudinal one in F1, and a global treatment [12,41,45] of the longitudinal and transverse components of the spin current and spin accumulation then requires the diffusive aspects of CPP-MR theory [28,51].

Acknowledgments: The authors thank Henri Jaffrès for spin-accumulation calculations, and N.O. Birge, P.M. Levy and M.D. Stiles for helpful suggestions. This research was supported by the MSU CFMR, CSM, Keck Microfabrication Facility, NSF grants DMR 02-02476, 98-09688, NSF-EU collaborative grant 00-98803 and Seagate Technology.

Table 3.1

Fig. #	F1/N/F2	F1	F1/N	F1(Net)	F2	N/F2	F2(Net)	MR	CIMS
1	Py/Cu/Py	+	+	+	+	+	+	+	+
2	Fe(Cr)/Cr/Fe(Cr)	-	-	-	-	-	-	+	-
3	Py/Cu/Cr/Fe(Cr)	+	+	+	-	-	-	-	+
4	Ni(Cr)/Cu/Py	-	+	-	+	+	+	-	-
5	Py/Cu/Ni(Cr)	+	+	+	-	+	-	-	+

Table 3.1: F1/N/F2 for each figure, giving: the spin anisotropies (+ = positive, - = negative) of F1, F1/N, and their net anisotropy F1(Net), those of F2, N/F2, and their net anisotropy F2(Net), and the signs of the observed MR and CIMS (+ = normal and - = inverse).

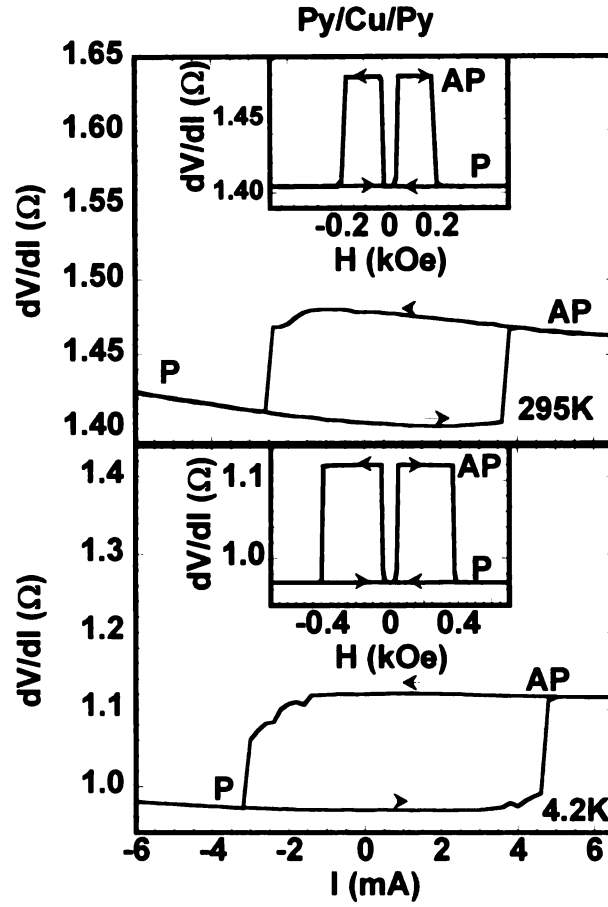


Fig. 3.1. Py(24)/Cu(10)/Py(6) data at 295K (top) and 4.2K (bottom) showing normal MR (dV/dI vs H at $I = 0$) in the insets and normal CIMS for dV/dI vs I in the main figures at $H = 0$ Oe for 295K and at $H = 20$ Oe for 4.2K. In all figures, $I > 0$ is always from F1 to F2.

Fe(Cr)/Cr/Fe(Cr)

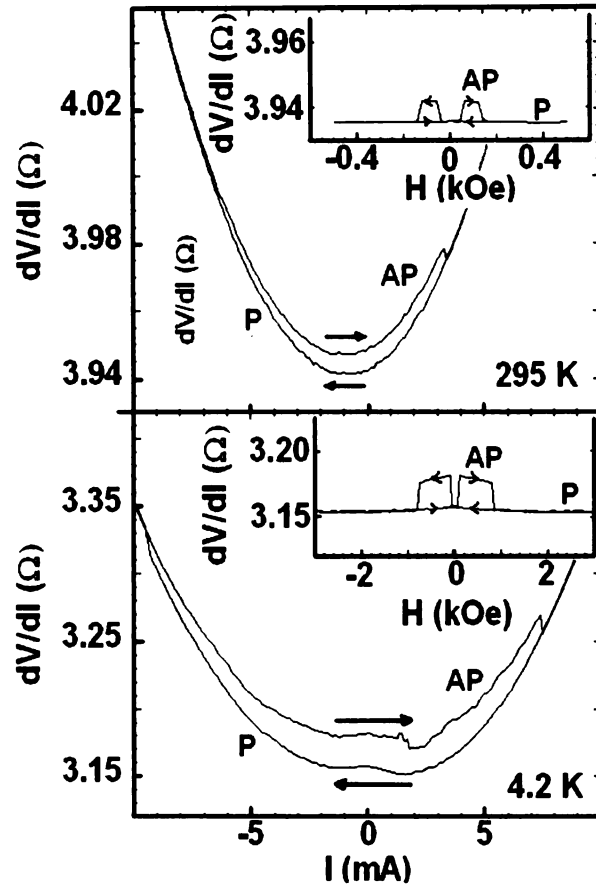


Fig. 3.2. Fe(Cr)(30)/Cr(6)/Fe(Cr)(3.5) data at 295K (top) and 4.2K (bottom) showing normal MR (dV/dI vs H at $I = 0$) in the insets but inverse CIMS for dV/dI vs I at $H = 0$ in the main figures.

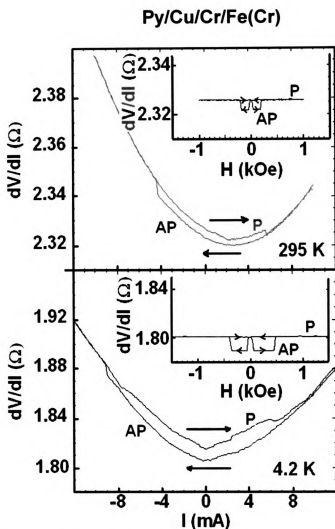


Fig. 3.3. Py(20)/Cu(7)/Cr(3)/Fe(Cr)(3) data at 295K (top) and 4.2K (bottom) showing inverse MR (dV/dI vs H at $I = 0$) in the insets but normal CIMS for dV/dI vs I at $H = 0$ in the main figures.

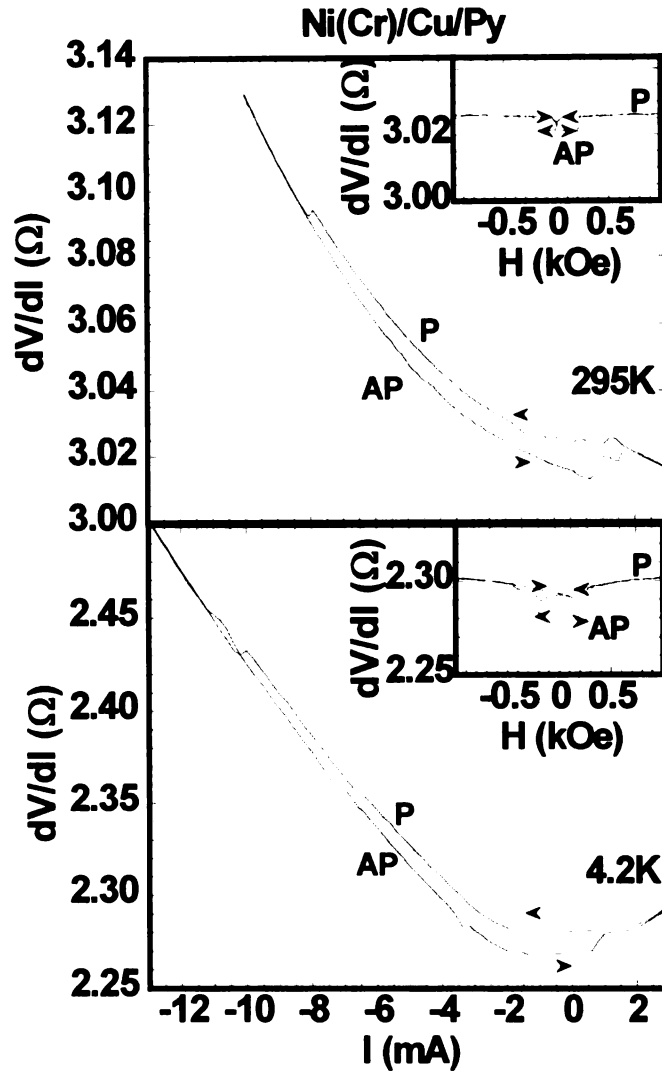


Fig. 3.4. Ni(Cr)(20)/Cu(20)/Py(10) data at 295K (top) and 4.2K (bottom) showing inverse MR (dV/dI vs H at $I = 0$) in the insets and inverse CIMS for dV/dI vs I at $H = 0$ in the main figures.

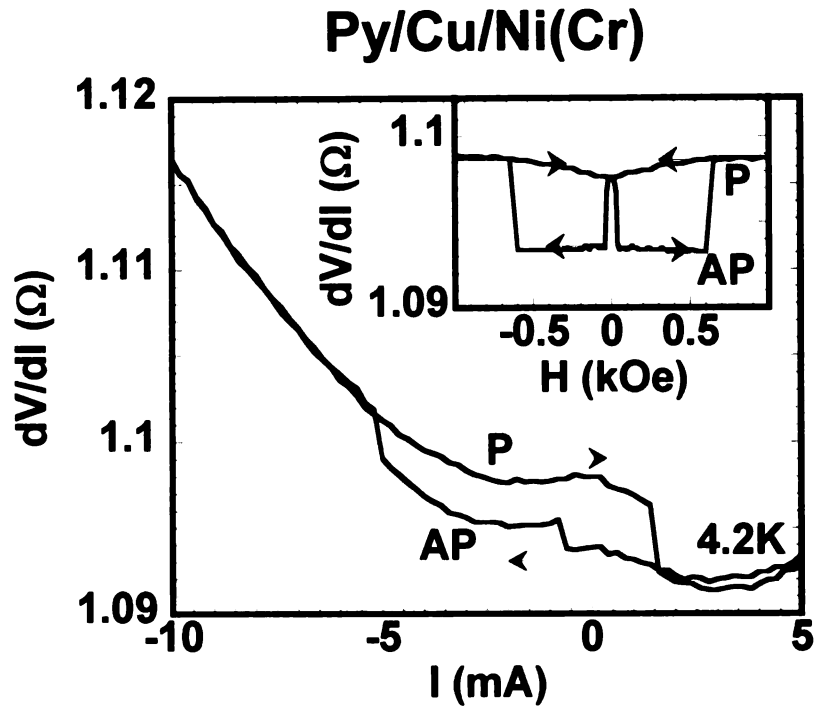


Fig. 3.5. Py(24)/Cu(10)/Ni(Cr)(4) data at 4.2K showing inverse MR (dV/dI vs H at $I = 0$) in the inset and normal CIMS for dV/dI at $H = 0$ Oe in the main figure.

Chapter 4. Spin-Transfer-Torque Generation of High Frequency (GHz) Radiation in Nanopillars: Sample Geometry, Measuring Systems, Data Taking, and Sample Data.

4.1. Background.

The first experimental evidence for generation of high frequency oscillations in F/N multilayers by a large current density was given in [5,6]. The first spectroscopic studies, such as those described in this chapter, were [52] for nanopillars and [53] for injection from a point contact into extended multilayers. When Mustafa began his PhD thesis research, our group had no experience with GHz measurements. We were, thus, pleased when Seagate invited him to work with them for one summer on early GHz studies. He was supervised there by Mark Covington, who was very pleased with Mustafa's work, which led to two papers [54,55].

After returning to MSU, Mustafa contributed to: (1) developing a sample geometry for GHz studies, (2) assembling a system for measuring such radiation at frequencies up to 12 GHz and using this system for taking some data, and (3) developing a system for measuring to frequencies up to 40 GHz. Unfortunately, he became incapacitated before he could use this latter system. We describe here each of these items, using figures prepared by Mustafa (with only occasional minor modifications for clarity), and providing only minimal connective material.

4.2 Sample Geometry.

Jointly with Irinel Chiorescu and Bill Pratt, Mustafa designed a sample geometry for GHz measurements. Together they decided that we could put six samples on a chip, with

each sample part of a coplanar waveguide to give a $50\ \Omega$ effective impedance as seen by a ‘picoprobe’ pair ($50\ \Omega$ miniature coaxial cable contact probes). Details of the sample structure are shown in Fig. 4.1. As the lithographic techniques for preparing nanopillar samples are similar to those described in the MSU PhD thesis of Huseyin Kurt (2005), we do not repeat them here.

Fig. 4.1 shows the final chosen sample geometry. Each chip contains six nanopillars as shown at the bottom left. Each nanopillar is at the center of four contacts (two grounded) as shown at the bottom right. This structure is in the center of a larger co-axial strip geometry shown in the upper middle. The picoprobe contacts can be connected either at the top or the bottom (both cases shown).

MSU Au-electrode configuration for making connections to nanopillars & nanocontacts

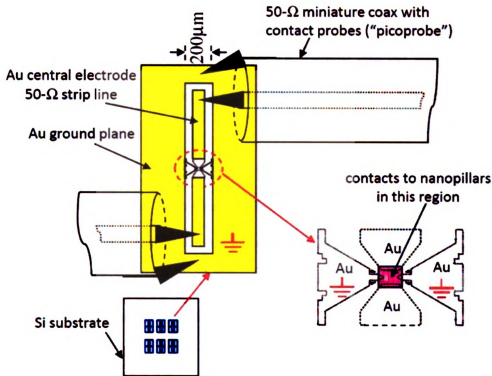


Fig. 4.1 Sample configuration for GHz measurements. Each Si substrate contains 6 samples (lower left). Each sample has four Au contacts (lower right). Two of these Au contacts are grounds and two constitute 50 Ω strip lines (upper figure). Each sample can be contacted by a picoprobe coaxial cable pair in two ways as illustrated at the top and bottom of the upper figure.

4.3 Measuring System to 12 GHz, Expected Behaviors, and Data.

4.3.1. The Measuring System to 12 GHz.

The measuring system for up to 12 GHz consists of the sample, R_L , a Bias T to allow simultaneous handling of input of a large DC current into the sample and emission of GHz radiation by the sample, and a pre-amplifier and a spectrometer to measure the emitted GHz radiation.

Fig. 4.2 shows schematic drawings of: a nanopillar (left), a sample with picoprobe attachment (center), and the system for measuring frequencies to 12 GHz (right). Since we have already discussed the nanopillar geometry in sections 2 and 3, and the sample geometry for GHz measurements in section 4.2, we focus in this section of chapter 4 on the measuring system and on data taken with it.

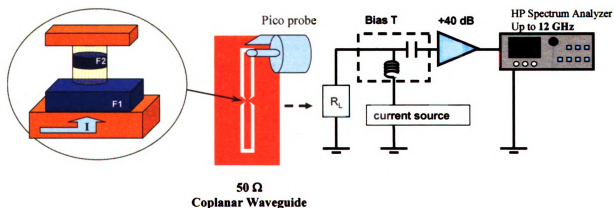


Fig. 4.2. Schematic drawings of a nanopillar (left), a sample with pico-probes (middle), and the system for measuring GHz radiation up to 12 GHz.

4.3.2 Expected Dynamical Motions.

The next issues are the dynamical motions and frequencies expected from the spin-torque model for assumed monodomain motion of the free (i.e., precessing) layer. Fig. 4.3 shows examples of trajectories of the magnetization of the ‘free’ layer, calculated by Mustafa, using a model by J.Z. Sun [56], of the dynamics expected for an F/N/F nanopillar subject to spin-transfer torque, assuming that the excited free layer remains monodomain.

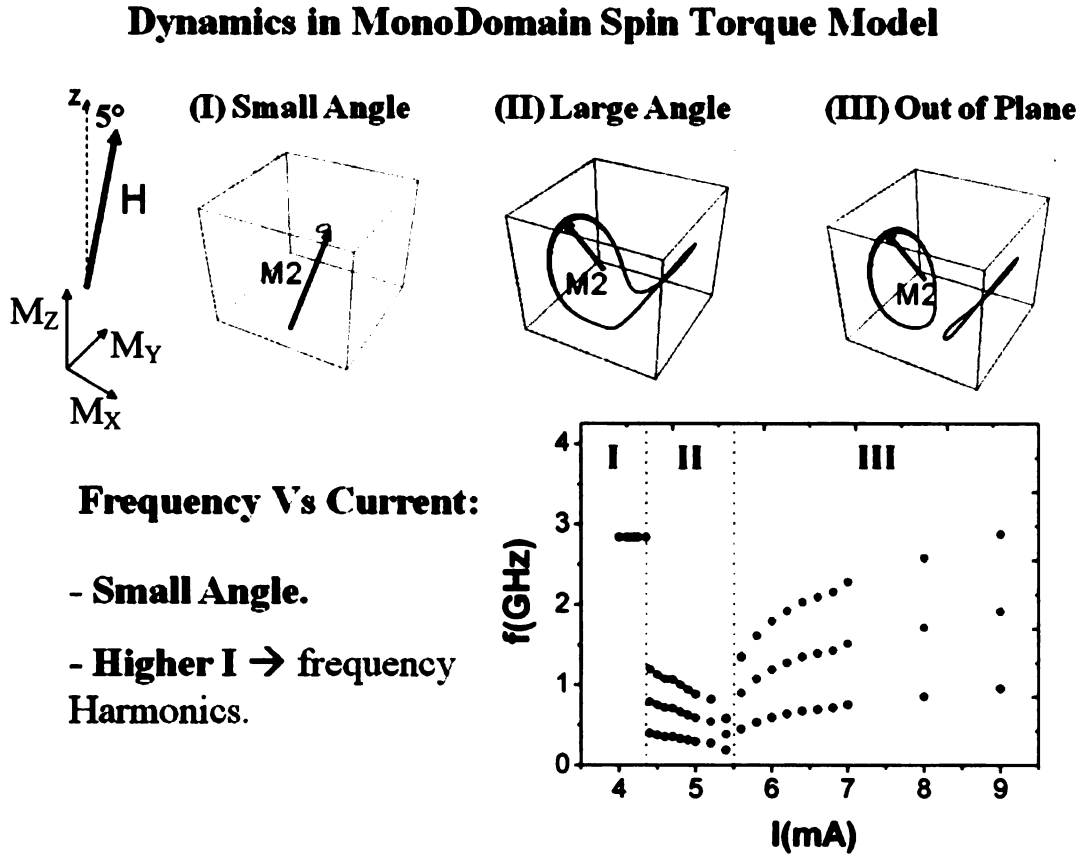


Fig. 4.3. The x,y,z scale, and the direction of application of the magnetic field (top left). Three different monodomain motions of the free layer magnetization (assumed monodomain) (top middle and right). Frequencies expected for different applied magnetic fields (lower right).

The motions such as those shown in Fig. 4.3 give rise to a predicted phase diagram vs H and I for monodomain precession of the free layer (including reversals at low enough H and I). Fig. 4.4 shows the phase diagram as functions of H (ordinate) and I (abscissa) expected from monodomain analysis such as in Fig. 4.3. Between I_{C-} and I_{C+} , the sample switches irreversible between parallel (P) and anti-parallel (AP) states. Examples of such behavior were shown in sections 2 and 3. For large enough positive I, and small H, the sample is driven into the AP state. For large enough magnitude negative I, and all H, the sample is driven into the P state. For large enough I and large enough H the sample is driven into dynamical states with motions such as shown in Fig. 4.3.

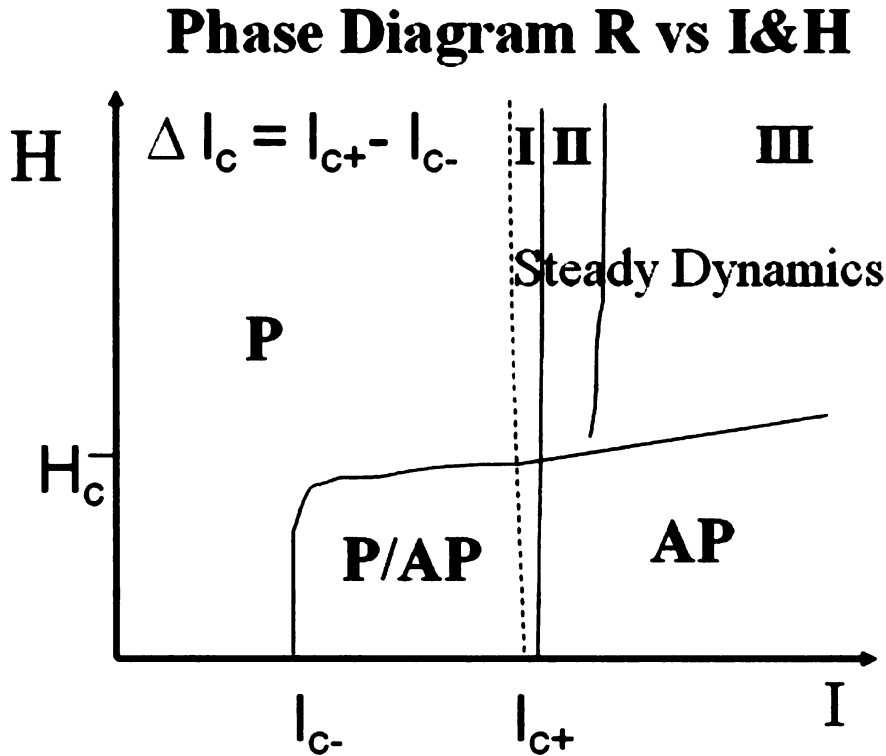


Fig. 4.4. Phase diagram as functions of applied magnetic field H (ordinate) and current I (abscissa) expected from monodomain analysis. I, II, and III correspond to the different motions shown in Fig. 4.3.

4.3.3. Experimental Data and an Example of Scaling.

Finally, we turn to examples of data, shown for two samples (#3 and #5) from chip #2b in Figs. 4.5 and 4.6. Comparison of the various parts of these figures shows general similarities for the two samples, but differences in details. Mustafa discovered that the similarities could be made clearer by comparing data at closely similar normalized values of H/H_C and $I/\Delta I_C$, where ΔI_C is the difference between the critical switching currents I_{C+} and I_{C-} , and H_C is the critical switching field, both indicated in Fig. 4.4. Normalized values for the two samples from chip #2b are shown in Fig. 4.7. He argued that such a result was consistent with the Landau-Lifshitz-Gilbert (LLG) equation including the Slonczewski (S) torque term as follows.

First, define \mathbf{m} as the unit vector along the direction of magnetization \mathbf{M} of the free (switching) F-layer, and \mathbf{m}' as the unit vector along the direction of \mathbf{M}' of the polarizing (fixed) F-layer. Also, define an effective magnetic field $\mathbf{H}_F = \mathbf{H}_{APP} + \mathbf{H}_{AN} + \mathbf{H}_D$, where \mathbf{H}_{APP} is the applied magnetic field, \mathbf{H}_{AN} is the in-plane anisotropy field, and \mathbf{H}_D is the demagnetizing field. Then the LLG-S equation can be written as [57,58]

$$d\mathbf{m}/dt = -\gamma_0 \mathbf{m} \times \mathbf{H}_F + \alpha(\mathbf{m} \times (d\mathbf{m}/dt)) + IK(\mathbf{m} \times \mathbf{m} \times \mathbf{m}'), \quad (4.1)$$

where I is the applied current and K is a constant that depends on known constants (such as the electron charge and Planck's constant) and a polarizing factor derived from the angular dependence of the Slonczewski spin-torque. If the F- and N-layers of two samples are the same metals, with the same nominal thicknesses, but with modestly different values of H_C and I_C due to subtle differences between the samples, then one might hope that normalizing \mathbf{H}_F by H_C , and I by ΔI_C , where H_C and I_C are defined in Fig.

4.4, would give a normalized Eq. 4.1 that corrects for these differences, resulting in 'scaling' behavior . Fig. 4.7 shows an example of such scaling.

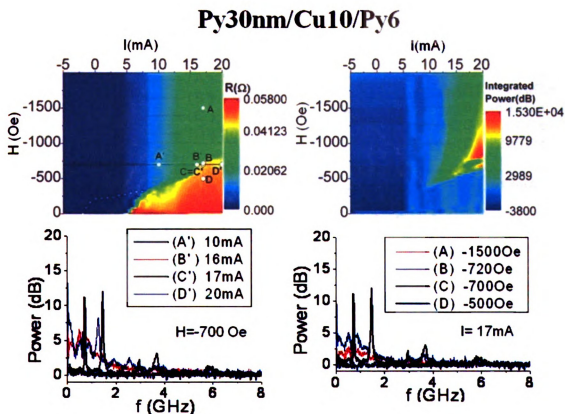


Fig. 4.5. GHz radiation data from sample #2b5. Top: Examples of experimental 'phase diagrams' showing MR (upper left) and integrated power (upper right) as functions of H and I . Bottom: Examples of GHz peaks for fixed $H = -700$ Oe and variable I (lower left) and for fixed $I = 17$ mA and variable H (lower right).

Py30nm/Cu10/Py6

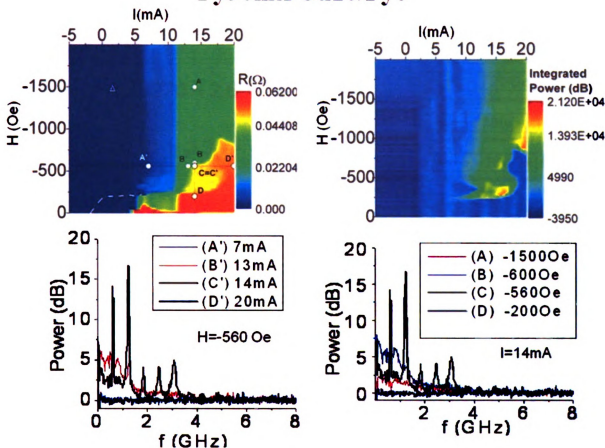


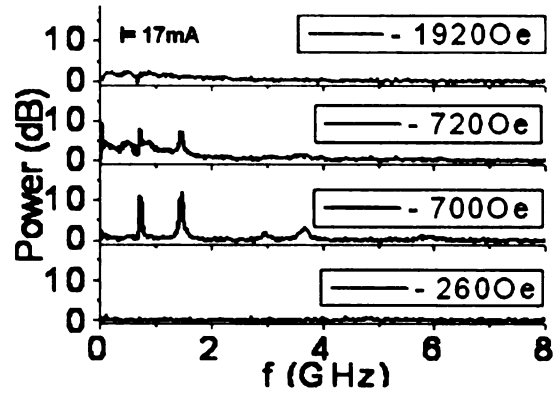
Fig. 4.6. GHz radiation data from sample #2b3. Top: Examples of experimental ‘phase diagrams’ showing MR (upper left) and integrated power (upper right) as functions of H and I. Bottom: Examples of GHz peaks for fixed H = - 560 Oe and variable I (lower left) and for fixed I = 14 mA and variable H (lower right).

Comparison

Sample #1 :

$$H/H_c \sim 700/270 \sim 2.60$$

$$I/\Delta I_c \sim 17/7.1 \sim 2.39$$



Sample #2 :

$$H/H_c \sim 560/210 \sim 2.66$$

$$I/\Delta I_c \sim 14/5.8 \sim 2.41$$

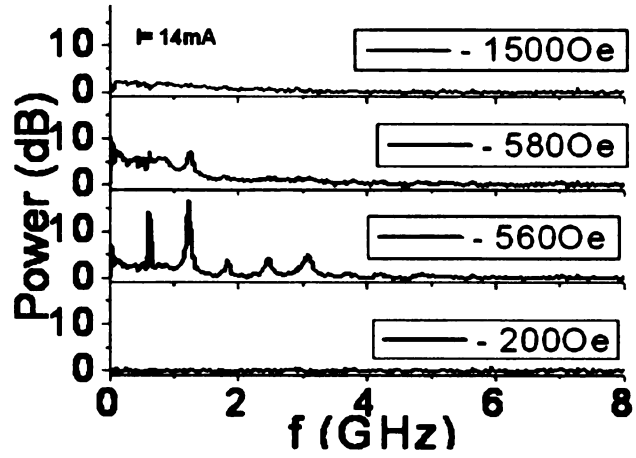


Fig. 4.7. Scaling Plots: Power versus frequency plots comparing spectra for sample #1 and #2 at normalized values of H/H_c and $I/\Delta I_c$.

4.4. System for measuring GHz radiation up to 40 GHz and Time Domain

studies.

We conclude this thesis by describing the system for measuring GHz radiation up to 40 GHz and for time domain studies, that Mustafa designed and constructed jointly with Irinel Chiorescu. As illustrated schematically in Fig. 4.8, for simple GHz studies, the system consists of: a microwave (MW) generator up to 40 GHz, a mixer, low-bandwidth amplifier, and a detector. The input signal from the sample is mixed with that from the MW generator, and the frequency of the latter is adjusted to obtain a difference signal at low enough frequency to be processed by the low bandwidth amplifier (~ 100 MHz) and a detector. As shown in Fig. 4.9, the detector could be an Acqiris oscilloscope operating in a Fast Fourier Transform (FFT) mode.

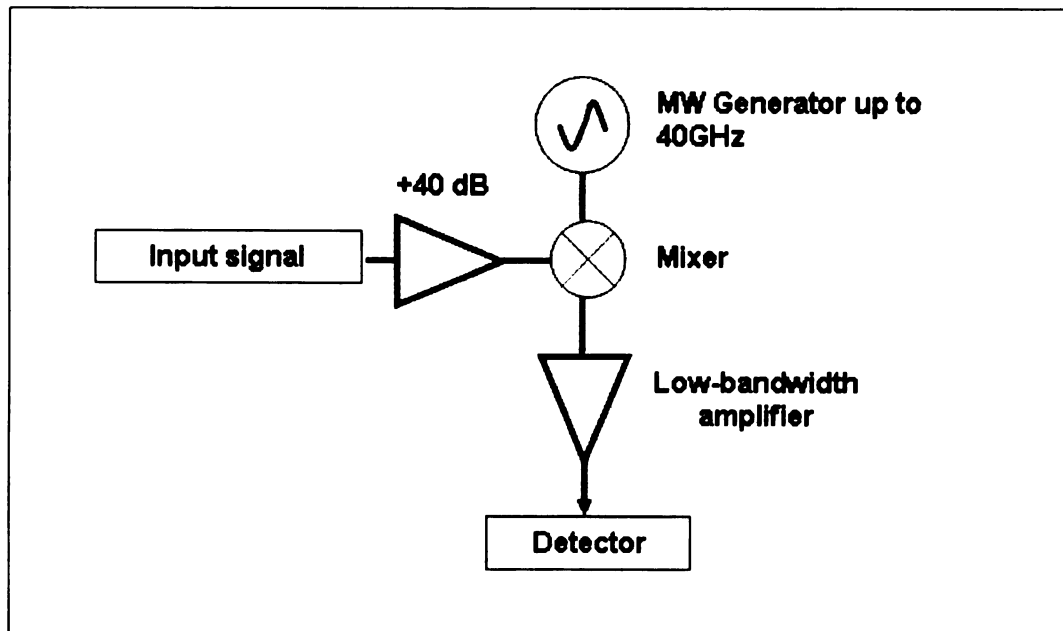


Fig. 4.8. Schematic of the system for studying current-generated signals to 40 GHz.

Fig. 4.9 shows details of the system of Fig. 4.8, along with the additional components needed for time domain studies. For simplicity, we have omitted GPIB connections that allow the computer to control the current to the electromagnet and the Anritsu 0.01-40 GHz oscillator, and also to the dc pulser and the Acqiris oscilloscope. Fig. 4.8, the frequency-spectrum mode, is obtained by setting the switches in Fig. 4.9 to position (1) on the right hand side and to position (2a) on the left hand side. The right-hand picoprobe is used to measure either the sample resistance (V/I) using a dc current, or dV/dI using a low frequency ac current and a lock-in amplifier, and also to insert the large dc current needed to generate the spin-torque and to carry out to the mixer the excited GHz radiation.

Contacting the sample with the left hand picoprobe, allows injection of a dc or microwave current pulse for time domain studies. In this case, the switches in Fig. 4.9 are set to position 2 on the right hand side and to either 2a or 2b on the left hand side. Such studies start with the computer sending a trigger signal to the Acqiris oscilloscope that in turn sends a trigger signal to the dc pulser (shown in Fig. 4.10). The output of the dc pulser is either sent through the bias-T (left switches in the '2a' position) as a current pulse to the left picoprobe, or directly (left switches in the '2b' position) to the microwave (MW) pulser (shown in Fig. 4.11). With the right switches in the '2' position, the transient output of the high bandwidth amplifier goes directly to the Acqiris oscilloscope and the continuous output of the Anritsu oscillator is connected to the MW pulser. The use of the Acqiris oscillator for both triggering and transient-signal acquisition generates less time 'jitter' between the trigger start and the display time-

sweep of the oscilloscope. Together, the Acqiris oscilloscope bandwidth of 2GHz, and sampling rate of 2G-samples/sec, are adequate for nanosecond time scale experiments.

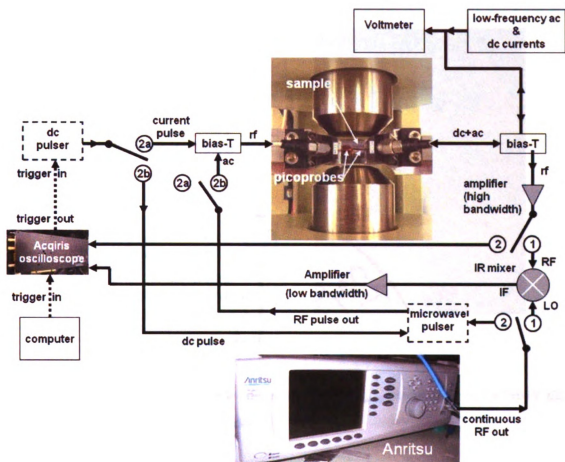


Fig. 4.9. Details of the system for both frequency studies to 40 GHz and time domain studies.

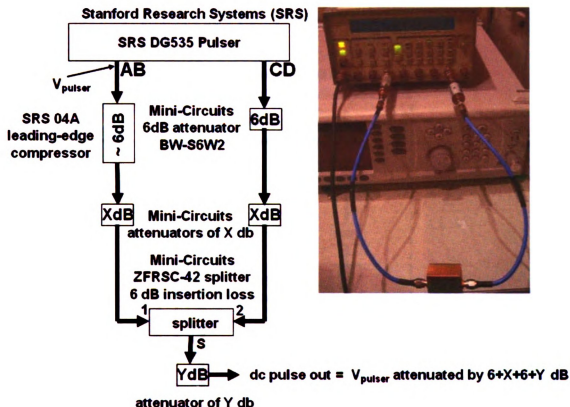


Fig. 4.10. DC Pulse Generator.

Fig. 4.10 shows the circuit for generating dc current-pulses. A voltage pulse (" V_{pulse} ") of desired duration leaves the AB-channel output and enters the leading-edge compressor, giving 0.1-ns rise time and ~ 2 -ns fall time. The signal passes through an attenuator of X dB and is combined at the splitter/combiner with the signal from the CD-channel output, which has been attenuated by the same amount as the AB signal. The edge compressor requires the AB channel output to be offset by ~ -1.65 V. The amplitude of the pulse on channel AB is $0.9\text{V} < V_{\text{pulse}} < 2.1$ V. To compensate the effect

of the offset on the final pulse, the offset of channel CD is tuned to + 1.6 V. Channel CD does not emit a pulse. Thus the splitter/combiner puts out a dc pulse with zero-offset that can then be attenuated by YdB.

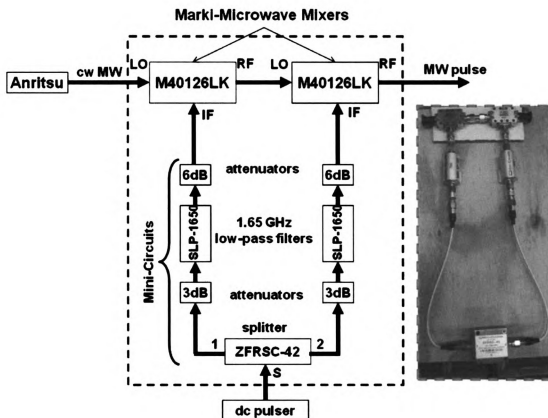


Fig. 4.11. Microwave (MW) Pulse Generator.

Fig. 4.11 shows the diagram for generating MW pulses. The output from the dc pulse circuit is divided by the splitter and fed via the attenuators and 1.65-GHz low-pass filters to two mixers. The mixers amplitude-modulate the continuous MW signal coming from the Anritsu oscillator;. These particular mixers operate at < 26 GHz, but operating frequencies up to 50 GHz are available from this manufacturer. In the off state, a mixer

will still pass some MW signal—the on/off-ratio ($r_{\text{ON/OFF}}$) is not infinite. To reduce this problem, two mixers are placed in series so that the overall on/off ratio is now $(r_{\text{ON/OFF}})^2$. The low-pass filters have a cutoff frequency $f_c = 1.65$ GHz, and the value of f_c obeys the following inequality: $(2\pi\tau)^{-1} < f_c < f_{\text{MW}}$ where τ is the desired rise time of the dc pulse and f_{MW} is the frequency of the MW signal. The attenuators should be set as high as possible, consistent with the mixers being able to open.

5. Summary and Conclusions.

This thesis contains results of studies of two related phenomena: (A) Current-Induced Magnetization Switching (CIMS), and (B) Current-Induced Generation of GHz Radiation.

(A) The CIMS part focuses upon two papers that report results of measurements of current-perpendicular-to-plane (CPP) magnetoresistance (MR) and CIMS behavior in Ferromagnetic/Non-metal/Ferromagnetic (F1/N/F2) nanopillars. It was shown that judicious combinations of F1 and F2 metals with different bulk scattering asymmetries, and with F1/N and N/F2 interfaces having different interfacial scattering asymmetries, could ‘invert’ both the CPP-MR and the CIMS, controllably and independently. In ‘normal’ CPP-MR, $R(AP) > R(P)$, where $R(AP)$ and $R(P)$ are the resistances in the anti-parallel (AP) and parallel (P) orientations of the F1 and F2 magnetic moments. In ‘normal’ CIMS, positive current switches the nanopillar from the P to the AP state. In ‘inverse’ CPP-MR, $R(P) > R(AP)$. In ‘inverse’ CIMS, positive current switches the nanopillar from the AP to the P state. All four possible combinations of CPP-MR and CIMS—(a) ‘normal’-‘normal’, (b) ‘normal’-‘inverse’, ‘inverse’-‘normal’, and (d) ‘inverse’-‘inverse’ were demonstrated and explained with carefully chosen combinations of F1, N, and F2. These results ruled out the self-Oersted field as a potential source of the switching, since the direction of the self-Oersted field does not depend upon the bulk or interfacial scattering asymmetries. By using carefully chosen impurities to reverse the bulk scattering asymmetry, the data showed also the importance of scattering off of impurities within the bulk F1 and F2 metals—i.e. that the transport must be treated as ‘diffusive’ rather than ‘ballistic’.

(B) The GHz studies consisted of five parts: (a) designing an appropriate sample geometry; (b) fabricating nanopillar samples in this geometry; (c) constructing a system for measurements up to 12 GHz and using it to obtain current-driven GHz radiation data; (d) providing a justification for ‘scaling’ behavior of GHz data for two nominally identical (but in practice subtly different) samples, and showing an example of such scaling; and (e) designing and constructing a system for measurements up to 40 GHz and for time domain studies.

BIBLIOGRAPHY

- [1] J. Slonczewski, J. Magn. Magn. Mater. **159**, L1 (1996).
- [2] J. Slonczewski, J. Magn. Magn. Mat.. **247**, 324 (2002).
- [3] L. Berger, Phys. Rev. **B54**, 9353 (1996).
- [4] L. Berger, J. Appl. Phys. **89**, 5521 (2001).
- [5] M. Tsoi, A.G.M. Jansen, J. Bass, W.-C. Chiang, M. Seck, V. Tsoi, P.W. Wyder, Phys. Rev. Lett. **80**, 4281 (1998); **81** 493 (E) (1998)
- [6] M. Tsoi, A.G.M. Jansen, J. Bass, W.-C. Chiang, V. Tsoi, P.W. Wyder, Nature (London) **406**, 46 (2000).
- [7] E.B. Myers, D.C. Ralph, J.A. Katine, R.N. Louie, R.A. Buhrman,, Science **285**, 867 (1999).
- [8] Ya. B. Bazaliy, B.A. Jones S.C. Zhang, J. Appl. Phys. **89**, 6793 (2001).
- [9] A. Brataas, Y. V. Nazarov, G.E.W. Bauer, Phys. Rev. Lett. **84**, 2481 (2000).
- [10] X. Waintal and P.W. Brouwer, Phys. Rev. **B63**, 220407 (2001).
- [11] C. Heide, Phys. Rev. **B65**, 054401 (2001).
- [12] M.D. Stiles and A. Zangwill; Phys. Rev. **B66**, 014407 (2002).
- [13] S. Zhang, P.M. Levy, A. Fert, Phys. Rev. Lett. **88**, 236601 (2002).
- [14] J.-E. Wegrowe, Phys. Rev. **B62**, 1067 (2000).
- [15] J.A. Katine, F.J. Albert, R.A. Buhrman, E.B. Myers, D.C. Ralph, Phys. Rev. Lett. **84**, 3149 (2000).
- [16] F.J. Albert, J.A. Katine, R.A. Buhrman, D.C. Ralph, Appl. Phys. Lett. **77**, 3809 (2000).
- [17] F.B. Mancoff and S.E. Russek, IEEE Trans. Magn. **38**, 2853 (2002).
- [18] J.Z. Sun, D.J. Monsma, D.W. Abraham, M.J. Rooks, R.H. Koch, Appl. Phys. Lett. **81**, 2202 (2002).
- [19] E.B. Myers, F.J. Albert, J.C. Sankey, E. Bonet, R.A. Buhrman, D.C. Ralph, Phys. Rev. Lett. **89**, 196801 (2002).
- [20] F.J. Albert, N.C. Emley, E.B. Myers, D.C. Ralph, R.A. Buhrman, Phys. Rev. Lett. **89**, 226802 (2002).

- [21] Y. Ji, C.L. Chien, and M.D. Stiles, Phys. Rev. Lett. **90**, 106601 (2003).
- [22] W.H. Rippard, M.R. Pufall, T.J. Silva, Appl. Phys. Lett. **82**, 1260 (2003).
- [23] J. Grollier, V. Cros, A. Hamzic, J.M. George, H. Jaffres, A. Fert, G. Faini, J. Ben Youssef, H. Le Gall, Appl. Phys. Lett **78**, 3663 (2001).
- [24] M.R. Pufall, W.H. Rippard, T.J. Silva, Appl. Phys. Lett. **83**, 323 (2003).
- [25] B. Oezylmaz, A.D. Kent, D. Monsma, J.Z. Sun, M.J. Rooks, R.H. Koch, Phys. Rev. Lett. **91**, 067203 (2003).
- [26] S. Urazhdin, N.O. Birge, W.P. Pratt Jr., J. Bass, Phys. Rev. Lett. **91**, 146803 (2003)
- [27] S. Urazhdin, H. Kurt, W.P. Pratt Jr., J. Bass, Appl. Phys. Lett. **83**, 114 (2003).
- [28] J. Bass and W.P. Pratt Jr., J. Magn. Magn. Mat. **200**, 274 (1999); Erratum **296**, 65 (2006)..
- [29] C. Vouille, A. Barthelemy, F. Elokani Mpondo, A. Fert, P.A. Schroeder, S.Y. Hsu, A. Reilly, R. Loloee, Phys. Rev. **B60**, 6710 (1999)
- [30] I. Mertig, R. Zeller, and P.H. Dederichs, Phys. Rev. **B47**, 16178 (1993).
- [31] I.A. Campbell and A. Fert, Ferromagnetic Materials, **3**, E.P. Wolforth, Ed., North-Holland, 1982, Pg. 747.
- [32] M.D. Stiles and D.R. Penn, Phys. Rev. **B61**, 3200 (2000).
- [33] K. Xia, P.J. Kelly, G.E.W. Bauer, I. Turek, J. Kudrnovsky, V. Drchal, Phys. Rev. **B63**, 064407 (2001).
- [34] J. Grollier, V. Cros, H. Jaffres, M.A. Hamzic, J.M. George, G. Faini, J. Ben Youssef, H. Le Gall, A. Fert, Phys. Rev. **B67**, 174402 (2003).
- [35] For additional experimental references see J. Bass, S. Urazhdin, N.O. Birge, W.P. Pratt Jr. Phys. Stat Sol. (a) **201**, No. 7, 1379 (2004).
- [36] Ya. B. Bazaliy, B.A. Jones, Shou-Cheng Zhang, Phys. Rev. **B57**, R3213 (1998).
- [37] X. Waintal, E.B. Myers, P.W. Brouwer, D.C. Ralph, Phys. Rev. **B62**, 12317 (2000).
- [38] C. Heide, P.E. Zilberman, R.J. Elliott, Phys. Rev. **B63**, 064424 (2001)
- [39] C. Heide, Phys. Rev. Lett. **87**, 197201 (2001).
- [40] Y. Tserkovnyak, A. Brataas, G.E.W. Bauer., Phys. Rev. **B66**, 224403 (2002).
- [41] M.D. Stiles and A. Zangwill, J. Appl. Phys. **91**, 6812 (2002)

- [42] J.-E. Wegrowe, D. Kelly, Y. Jaccard, Ph. Guittienne, and J. Ph. Ansermet, Europhys. Lett. **45**, 626 (1999);
- [43] J.-E. Wegrowe, X. Hoffer, Ph. Guittienne, A. Fabian, L. Gravier, T. Wade, J. Ph. Ansermet, J. Appl. Phys. **91**, 6806 (2002).
- [44] S. Urazhdin, Phys. Rev. **B69** 134430 (2004).
- [45] A. Fert, V. Cros, J.-M. George, J. Grollier, H. Jaffres, A. Hamzic, A. Vaures, G. Faini, J. Ban Youssef, H. Le Gall, J. Mag. Mat. **272-276**, 1706 (2004).
- [46] M. AlHajDarwish, A. Fert, W.P. Pratt Jr., J. Bass, J. Appl. Phys. **95**, 6771 (2004).
- [47] A. Zambano, E. Eid. R. Loloe, W.P. Pratt Jr., J. Bass, J. Magn. Magn. Mat. **253**, 51 (2002).
- [48] I. Mertig, P. Zahn, M. Richter, H. Eschrig, R. Zeller, P.H. Dederichs, J. Magn. Magn. Mat. **151**, 363 (1995).
- [49] J. Barnas, A. Fert, M. Gmitra, I. Weymann, V.K. Dugaev, Phys. Rev. **B72**, 024426 (2005).
- [50] W. Park, R. Loloe, J.A. Caballero, W.P. Pratt Jr., P.A. Schroeder, J. Bass, A. Fert, C. Vouille, J. Appl. Phys. **85**, 4542 (1999).
- [51] T. Valet and A. Fert, Phys. Rev. **B48**, 7099 (1993).
- [52] S.I. Kiselev, J.C. Sankey, I. N. Krivorotov, N.DC. Emley, R.J. Schoelkopf, R.A. Buhrman, D.C. Ralph, Nature **425**, 380 (2003).
- [53] W.H. Rippard, M.R. Pufall, S. Kaka, S.E. Russek, T.J. Silva, Phys. Rev. Lett. **92**, 027201 (2004).
- [54] M. Covington, M. AlHajDarwish, Y. Ding, N.J. Gokemeijer, and M.A. Seigler, Phys. Rev. **B69**, 184406 (2004).
- [55] Spin Transfer Effects in Current perpendicular to the Plane Spin Valves, M. Covington, M. AlHajDarwish, Y. Ding, A. Rebei, G.J. Parker, N.J. Gokemeijer, and M.A. Seigler, J. Magn. Magn. Mat. **287**, 325 (2005).
- [56] J.Z. Sun, Phys. Rev. **B62**, 570 (2000).
- [57] O. Boulle, V. Cros, J. Grollier, L.G. Pereira, C. Deranlot, F. Petroff, G. Faini, J. Barnas, A. Fert, Phys. Rev. **B77**, 174403 (2008).
- [58] D.C. Ralph and M.D. Stiles, J. Magn. Magn. Mat. **320**, 1190 (2008).

MICHIGAN STATE UNIVERSITY LIBRARIES



3 1293 02956 7819